

PSFC/JA-13-52

Non-local Heat Transport in Alcator C-Mod Ohmic L-Mode Plasmas

C. Gao¹, J.E. Rice¹, H.J. Sun^{2,3}, M.L. Reinke¹, N.T. Howard¹,
D. Mikkelsen⁴, A.E. Hubbard¹, M.A. Chilenski¹, J.R. Walk¹,
J.W. Hughes¹, P.C. Ennever¹, M. Porkolab¹, A.E. White¹, C. Sung¹,
L. Delgado-Aparicio⁴, S.G. Baek¹, W.L. Rowan⁵, M.W. Brookman⁵,
M.J. Greenwald¹, R.S. Granetz¹, S.W. Wolfe¹, E.S. Marmor¹,
Alcator C-Mod Team¹

¹Plasma Science and Fusion Center, MIT, Cambridge, MA 02139, USA

²World Class Institute Center for Fusion Theory, National Fusion Research Institute, Daejeon 305-333, Korea

³South Western Institute of Physics, Chengdu 610041, Peoples Republic of China

⁴Princeton Plasma Physics Laboratory, Princeton, NJ 08543, USA

⁵Institute for Fusion Studies, University of Texas at Austin, TX 78712, USA

December, 2013

**Plasma Science and Fusion Center
Massachusetts Institute of Technology
Cambridge MA 02139 USA**

This work was supported by US DoE Contract No DE-FC02-99ER54512 and in part by an appointment to the US DOE Fusion Energy Postdoctoral Research Program administered by ORISE. Reproduction, translation, publication, use and disposal, in whole or in part, by or for the United States government is permitted.

Submitted for publication in *Nuclear Fusion*.

Non-local Heat Transport in Alcator C-Mod Ohmic L-Mode Plasmas

C. Gao¹, J.E. Rice¹, H.J. Sun^{2,3}, M.L. Reinke¹, N.T. Howard¹,
D. Mikkelson⁴, A.E. Hubbard¹, M.A. Chilenski¹, J.R. Walk¹,
J.W. Hughes¹, P.C. Ennever¹, M. Porkolab¹, A.E. White¹, C.
Sung¹, L. Delgado-Aparicio⁴, S.G. Baek¹, W.L. Rowan⁵, M.W.
Brookman⁵, M.J. Greenwald¹, R.S. Granetz¹, S.W. Wolfe¹,
E.S. Marmor¹, Alcator C-Mod Team¹

¹Plasma Science and Fusion Center, MIT, Cambridge, MA 02139, USA

²World Class Institute Center for Fusion Theory, National Fusion Research Institute,
Daejeon 305-333, Korea

³South Western Institute of Physics, Chengdu 610041, Peoples Republic of China

⁴Princeton Plasma Physics Laboratory, Princeton, NJ 08543, USA

⁵Institute for Fusion Studies, The University of Texas at Austin, Austin, TX 78712,
USA

E-mail: cgao@psfc.mit.edu

Abstract. Non-local heat transport experiments were performed in Alcator C-Mod Ohmic L-mode plasmas by inducing edge cooling with laser blow-off impurity (CaF₂) injection. The non-local effect, a cooling of the edge electron temperature with a rapid rise of the central electron temperature, which contradicts the assumption of “local” transport, was observed in low collisionality linear Ohmic confinement (LOC) regime plasmas. Transport analysis shows this phenomenon can be explained either by a fast drop of the core diffusivity, or the sudden appearance of a heat pinch. In high collisionality saturated Ohmic confinement (SOC) regime plasmas, the thermal transport becomes local: the central electron temperature drops on the energy confinement time scale in response to the edge cooling. Measurements from a high resolution imaging x-ray spectrometer show that the ion temperature has a similar behavior as the electron temperature in response to edge cooling, and that the transition density of non-locality correlates with the rotation reversal critical density. This connection may indicate the possible connection between thermal and momentum transport, which is also linked to a transition in turbulence dominance between trapped electron modes (TEMs) and ion temperature gradient (ITG) modes. Experiments with repetitive cold pulses in one discharge were also performed to allow Fourier analysis and to provide details of cold front propagation. These modulation experiments showed in LOC plasmas that the electron thermal transport is not purely diffusive, while in SOC the electron thermal transport is more diffusive like. Linear gyrokinetic simulations suggest the turbulence outside $r/a=0.75$ changes from TEM dominance in LOC plasmas to ITG mode dominance in SOC plasmas.

1. Introduction

For magnetically confined plasmas, it is still challenging to understand heat transport fully, which is important for predictions of the performance of burning plasma tokamaks like ITER. One of these challenges is the explanation of the non-local phenomenon: a fast response in a region of the plasma which is distant from a perturbation. The most famous example of the non-local effect in electron heat transport is the inward propagation of edge cooling. The first experiment was carried out on TEXT about 20 years ago [1, 2, 3], in which carbon was injected into the edge plasma to induce a temperature perturbation. The edge temperature decreased rapidly as expected, but interestingly the core temperature promptly began to rise, and peaked within a few milliseconds. This effect cannot be explained by the local transport model which assumes that transport coefficients are functions of local thermodynamic parameters. Similar effects have been observed in TFTR [4, 5], RTP [6, 7, 8], ASDEX Upgrade [9], Tore Supra [10], JET [11], LHD [12, 13, 14, 15], JT-60U [16, 17, 15], HL-2A [18, 19], Alcator C-Mod [20], etc. An interesting observation in these experiments is that the non-local effect disappears with increasing electron density. This critical cutoff density exists universally, although its value varies for different tokamaks depending on q and major radius. For example in TFTR [5] ($R_0 = 2.36$ m, $a = 0.71$ m, $B_t = 4.9$ T) the cutoff density was found to scale as $n_e(0)/\sqrt{T_e(0)} \leq 0.035 \times 10^{19} \text{ m}^{-3}/\text{eV}^{1/2}$, in RTP [7] ($R_0 = 0.72$ m, $a = 0.164$ m, $B_t \leq 2.4$ T, $I_p \leq 150$ kA) the cutoff line-averaged density is $2.7 \times 10^{19} \text{ m}^{-3}$, in ASDEX Upgrade [9] ($R_0 = 1.65$ m, $a = 0.5$ m, $\kappa = 1.6$, $B_t = 2.46$ T, $I_p = 600$ kA) the value is $1.8 \times 10^{19} \text{ m}^{-3}$, in Tore Supra [10] ($R_0 = 2.31$ m, $a = 0.75$ m, $B_t = 3.7$ T) the cutoff density was found to scale as $\langle n_e \rangle / I_p^2 \leq 1.0 \times 10^{19} \text{ m}^{-3} \text{ MA}^{-1/2}$, in HL-2A [19] ($R_0 = 1.65$ m, $a = 0.4$ m, $B_t = 1.45$ T, $I_p = 190$ kA) the value is $1.5 \times 10^{19} \text{ m}^{-3}$ and in Alcator C-Mod [20] ($R_0 = 0.67$ m, $a = 0.21$ m, $B_t = 5.4$ T), the critical density is $\sim 0.6 \times 10^{20} \text{ m}^{-3}$ for $I_p = 0.55$ MA ($q_{95} \sim 5.8$), $\sim 0.8 \times 10^{20} \text{ m}^{-3}$ for $I_p = 0.8$ MA ($q_{95} \sim 4.2$) and $\sim 1.3 \times 10^{20} \text{ m}^{-3}$ for $I_p = 1.1$ MA ($q_{95} \sim 3.3$).

The existence of a critical density for the non-local effect makes us consider the possible connection of nonlocality with the other phenomena. One of them is the transition from the linear ohmic confinement (LOC, also called neo-Alcator scaling) regime to the saturated ohmic confinement (SOC) regime [21, 22, 23, 24, 25, 26, 27, 28, 29, 30, 31, 32, 20]. It was found in Ohmic L-mode plasmas, the energy confinement time scales linearly with electron density and saturates as the density increases above some value. One hypothesis for the saturated performance is the change from trapped electron mode (TEM) dominant turbulent transport at low collisionality to ion temperature gradient (ITG) mode dominant turbulent transport at high collisionality. Another observation is the abrupt switch of direction of the plasma core rotation, from co-current to counter-current, without significant change of other macroscopic plasma parameters [33, 34, 31, 32, 20]. The change of direction (also called rotation reversal) is an example of momentum transport bifurcation, and is caused by changes in collisionality through the electron density, plasma current, magnetic field and configuration. Shown in Fig. 1

is the product of non-locality cutoff density and boundary safety factor (q_{95} for diverted plasmas and $q(a)$ for limited plasmas) as a function of major radius for different devices. The boundary safety factor is estimated by $q_{95} = \frac{5a^2 B_T}{R I_{MA}} \frac{1+\kappa^2}{2} \frac{1.17-0.65\epsilon}{(1-\epsilon^2)^2}$ [35] where $\epsilon = a/R_0$ is the inverse of aspect ratio. Fig. 1 shows that the collisionality ν_* , the ratio of collision frequency to bounce frequency ($\nu_* = 0.0118qRZ_{eff}n_e/T_e^2\epsilon^{1.5} \propto n_eqR$), could be a unifying parameter for the non-local effect. We ignore the factor of Z_{eff}/T_e^2 because it turns out that this factor is a weakly varying function of density [32]. The connection among the LOC-SOC transition, rotation reversal and a change in turbulence characteristics has been demonstrated [31, 32, 20, 36].

The goal of the experiments presented in this paper is to add the non-local to local transition to this list. Some of the experimental results can be found in [20]. In this paper we will emphasize the results of repetitive cold pulse injection experiments, some fluctuation observations, and numerical simulations. The remainder of this paper is organized as follows. In section 2, the experimental setup and data processing methods are described. In section 3, the experimental results will be presented. The discrepancy between propagation of cold pulses at low and high densities will be shown, as well as the changes in energy confinement and plasma rotation. The Fourier transform of electron temperature in repetitive cold pulses experiments will give more insight into the cold pulse propagation and the non-local effect. In section 4, we give a descriptive explanation of the non-local effect in low density L-mode plasmas in Alcator C-Mod. A sudden drop of core electron heat diffusivity can reproduce the experimental observation; the sudden appearance of a heat pinch models the results equally well. This cold pulse induced transient ITB-like state is augmented by core fluctuation measurements. In section 5, the results of linear gyrokinetic simulations of low and high density plasmas are presented. We see an obvious difference in the turbulence characteristics, which can be described as TEM dominant at low density and ITG mode dominant at high density. Conclusions and a discussion are presented in section 6.

2. Experimental setup, data processing methods

The experiments were carried out in Ohmic L-mode plasmas in the Alcator C-Mod tokamak [37] with major radius $R \sim 0.67$ m and minor radius $a \sim 0.21$ m. Typical Alcator C-Mod L-mode discharges are performed in lower single null (LSN) deuterium plasmas, $B_t = 5.4$ T, $I_p = 0.8$ MA, $\kappa \sim 1.7$, and line averaged electron density from 0.4 to 1.3×10^{20} m⁻³. Fig. 2 shows the cross-section of Alcator C-Mod during a typical LSN discharge.

2.1. Laser blow-off system

In Alcator C-Mod, a laser blow-off (LBO) system is used to study particle/impurity transport [38] by introducing non-intrinsic non-recycling impurities. The system includes a 0.68 J Nd Yag laser with pulse rate up to 10 Hz, coupled with fast beam

steering via a 2D piezoelectric mirror mount able to move spot locations in the 100 ms between laser pulses. A remotely controllable optical train allows the ablated spot diameter to vary from 0.5 to 7.0 mm. A small spot size is preferred for particle/impurity transport studies to avoid perturbation of background plasmas. For our experiments which require edge temperature perturbations, but minimal density perturbation, a medium spot size (~ 3 mm) is preferred. $2 \mu\text{m}$ of CaF_2 is used as the ablated material deposited on a thin film. A spot size of 2.5 mm will consist of approximately 10^{18} particles with a CaF_2 density of 3.18 g/cm^3 . Previous results indicate around 10% of the ablated particles will actually make it into the plasma in a typical L-mode [38].

2.2. Diagnostics

The electron temperature T_e profiles are measured by three ECE systems: GPC1 (grating polychromator) with 9 channels, GPC2 with 19 channels and FRCECE with 32 channels [39]. Most of the T_e results presented here were from the GPC1 system, whose typical time resolution is $10 \mu\text{s}$, with low noise levels of $\sim 10 \text{ eV}$ [39], which is sufficient for the study. The electron density profiles are measured by a Thomson scattering system [40, 41, 42, 43]. Line averaged density is measured by a two color interferometer [44]. Ion temperature and plasma rotation profiles are measured with a high resolution imaging x-ray spectrometer [45, 46]. Fluctuation measurements presented in this paper are made by phase contract imaging (PCI) [47, 48] and reflectometer systems [49].

2.3. Fourier analysis

The Fourier transform is a general technique to determine the phase and amplitude profile of a perturbation in a modulation experiment [50]. It is a common method for the study of transient transport and provides a high signal to noise ratio. For slab geometry and purely diffusive transport, electron heat diffusivity can be calculated separately from amplitude and phase profiles [51]: $\chi_e^{HP,amp} = \frac{3}{4}\omega / \left(\frac{A'}{A}\right)^2$ and $\chi_e^{HP,phase} = \frac{3}{4}\omega / \left(\frac{\varphi'}{\varphi}\right)^2$, where A is the Fourier transformed amplitude and φ is the phase. Due to damping [9] (from changes of local Ohmic power, electron-ion exchange and radiation), it usually obtains that $\chi_e^{HP,phase} > \chi_e^{HP,amp}$, and they converge at higher frequency. The convective effect can be observed in the amplitude profile and it will decrease with frequency. The phase profile is not sensitive to convection.

2.4. Generalized singular value decomposition

One difficulty we encountered in the experiments is the presence of sawtooth activity. Large amplitude sawteeth of $\sim 100 \text{ eV}$ in the core electron temperature occurred during the cold pulse experiments, which contaminates the quality of transient measurements. Repetitive injections and Fourier analysis improve the signal to noise level under the assumption that there is no strong interaction between sawtooth activity and the edge perturbations. The generalized singular value decomposition (GSVD) technique is used

to verify this assumption. A detailed description of this method applied to perturbation experiments has been made in [52]. The basic idea is to separate the sawtooth and perturbation signals by reconstructing the data in phase space. Assume $\mathbf{U}(\mathbf{x}, t)$ is the electron temperature signal measured from ECE before the perturbation which is dominated by sawtooth activity, and $\mathbf{Y}(\mathbf{x}, t)$ is that after the perturbation, whose evolution consists of both sawtooth activity and perturbation propagation. The GSVD gives \mathbf{U} and \mathbf{Y} a set of common bases. This set of bases is optimized such that some bases will best represent \mathbf{Y} and have little information on \mathbf{U} . The set of bases consists of both spatial and temporal modes. Signals \mathbf{U} and \mathbf{Y} share the same spatial modes $\mathbf{V}_k(\mathbf{x})$, but different temporal modes $A_k(t)$ for \mathbf{U} and $B_k(t)$ for \mathbf{Y} . The choice of bases is made as follows:

$$\mathbf{U}(\mathbf{x}, t) = \sum_{k=1}^K \alpha_k \mathbf{A}_k^*(t) \mathbf{V}_k(\mathbf{x}) \quad (1a)$$

$$\mathbf{Y}(\mathbf{x}, t) = \sum_{k=1}^K \beta_k \mathbf{B}_k^*(t) \mathbf{V}_k(\mathbf{x}) \quad (1b)$$

The temporal modes are orthonormal and weights are normalized, i.e., $\langle \mathbf{A}_m^* \cdot \mathbf{A}_n \rangle = \langle \mathbf{B}_m^* \cdot \mathbf{B}_n \rangle = \sigma_{mn}$ and $\alpha_m^2 + \beta_m^2 = 1$. Spatial modes are not necessary to be orthonormal, generally $\langle \mathbf{V}_m^* \cdot \mathbf{V}_n \rangle \neq 0$ for $m \neq n$. If the sawtooth and perturbation are not strongly coupled, only a few modes will be able to recover the perturbation signal with removal of sawtooth activity. The GSVD method will quantitatively determine how strong the two signals are coupled, as well as separating them in a self-consistent way.

3. Experimental results

Fig. 3 shows selected time traces from a typical SOC L-mode discharge with a cold pulse: $B_t = 5.4$ T, $I_p = 0.8$ MA ($q_{95} \sim 4.2$), line averaged density $\langle n_e \rangle = 1.3 \times 10^{20} \text{ m}^{-3}$. Notice the core plasma rotation is in the counter-current direction (~ -30 km/s). The CaF_2 injection time is 0.8 s (dashed line). Following the edge cooling, the edge electron temperature drops immediately, as expected. The core electron temperature gradually decreases on a time scale of around 20 ms, which is comparable to the energy confinement time ~ 27 ms. In Fig. 4 the dashed line with the arrow shows the trajectory of minima in the electron temperature at different radii. The evolution of minima at different radii clearly shows the diffusive behavior of the cold front propagation. The core ion temperature also drops following the edge cooling.

Fig. 5 is an LOC L-mode discharge with the same parameters as Fig. 3 except for lower density $0.6 \times 10^{20} \text{ m}^{-3}$. The core plasma rotation is now in the co-current direction (~ 15 km/s). The CaF_2 injection time is 1.0 s. The core electron temperature begins to increase, rather than decrease, within 5 ms and peaks within 10 ms after the injection. This time scale is much less than the energy confinement time (~ 25 ms) and cannot be explained with a change of transport coefficients as a result of modification of local plasma parameters due to the edge cooling. In Fig. 6, for the outer plasma region it

takes a longer time to peak as the cold pulse propagates inwards; for the inner region, the time-to-peak decreases, which contradicts the pure diffusive transport. The core ion temperature also increases after the edge cooling, but peaks and decays on a longer time scale. Fig. 7 shows the profile evolution of the electron and ion temperatures during the LBO injection in the same LOC plasma. At 1.01 s the core ion temperature doesn't change within the uncertainty, while the core electron temperature peaks. At 1.03 s the core electron temperature drops, which is evidence that the cold front propagates to the core plasma; the edge electron temperature returns to its pre-injection value and the core ion temperature rises.

Figs. 8 and 9 are repetitive LBO injection experiments with similar plasma parameters ($B_t = 5.4$ T, $I_p = 0.8$ MA, $q_{95} \sim 4.2$) as in Figs. 3 and 5, respectively. Fig. 8 is an SOC discharge with line averaged density $\sim 1.05 \times 10^{20} \text{ m}^{-3}$ and counter-current directed rotation (~ -10 km/s). Fig. 9 is an LOC discharge with line averaged density $\sim 0.58 \times 10^{20} \text{ m}^{-3}$ and co-current directed core plasma rotation (~ 7 km/s). The CaF_2 injection rate is 10 Hz. Although the core electron temperature signals are contaminated by sawtooth activity, it is visible that for the SOC discharge, the core T_e drops with edge cooling and for the LOC discharge, the core T_e increases. To verify this observation and to extract the amplitude and phase profiles, GSVD was applied to the raw data. Fig. 10 is the result of the decomposition applied to the LOC discharge between 0.85 – 0.95 s with one injection event. Temporal modes $A_k(t)$, $B_k(t)$ and spatial modes $V_k(R)$ are calculated from electron temperatures with mean normalization, so they are dimensionless. It is shown that the first 2 modes can quantitatively represent the pulse process with sawtooth activity reduced by around 80% (the sawtooth amplitude reduced from ~ 500 eV before GSVD was applied to ~ 100 eV after GSVD was applied, as shown in Fig. 10(d)). Fig. 11 shows the LOC discharge (Fig. 9) temperature time traces with GSVD applied. Although it is impossible to remove totally the sawtooth activity, the increase of the core temperature is more clear for the three core channels. Fig. 12(a) is the result of Fourier transforms of the electron temperature for the discharge shown in Fig. 9 with GSVD applied. The first three harmonics of FFT profiles are shown. The location with minimum amplitude and phase crossing 90° indicates the “inversion radius”, which is around 0.78 m in major radius ($r/a \sim 0.5$). The amplitude of the first harmonic increases towards the core. This increase contradicts the assumption of purely diffusive transport. This modulation experiment result in LOC plasmas differs from previous single injection experiment (Figs. 5 and 6) in two regards. The first is that in the modulation experiment, there is no evidence that the cold front propagates into the core plasma. The other difference is the relative amplitude of changes in core and edge electron temperatures. In the modulation experiments, the amplitude of the core temperature increase is about twice the amplitude of the edge temperature drop (Figs. 11 and 12). For the single injection experiment (Figs. 5 and 6) the edge temperature has a larger perturbation than in the core. This discrepancy could be caused by the difference of ablated spot size. A larger injection would cause a larger perturbation in the edge and the cold pulse would propagate deeper into the core plasma. Fig. 12(b) is the FFT result

of the SOC discharge shown in Fig. 8 with GSVD applied. The amplitude decreases as the cold pulse propagates into the core, which suggests a purely diffusive process.

For the LOC discharge, where the non-local effect of edge cooling exists, it is found from PCI that the density fluctuations are suppressed during the injections, as shown in the first frame of Fig. 13. PCI provides a line integral measurement of density fluctuations. Fig. 14 is the time history of the spectral power integrated over 10 – 40 kHz, which clearly shows the turbulence suppression associated with the cold pulses. To identify the location of turbulence suppression, density fluctuations measured by the reflectometer at $r/a \sim 0.9$ are shown in the second frame of Fig. 13. There is no clear correlation between the fluctuations from the reflectometer and CaF_2 injections, so it should be the turbulence at least inside $r/a \sim 0.9$ which is suppressed instead of the edge turbulence [19]. The turbulence changes in the reflectometer are probably due to the density perturbations caused by injections, and a shift of the cutoff layer. We did not observe the suppression in SOC discharges when the cold pulse propagates diffusively and local transport is valid.

The recent experiments in LHD [53] show that the amplitude of the electron temperature fluctuations decreased and their radial correlation lengths shortened during the transient phase induced by pellet injection. In Alcator C-Mod the electron temperature fluctuation and correlation length can be measured using upgraded multi-channel CECE [54]. This will be an interesting topic for future experiments.

For LOC plasmas the core electron temperature increases almost linearly with the edge cooling, as shown in Fig. 15(a), where the changes of the core T_e ($r/a \sim 0.3$) are plotted as a function of drops in the edge T_e ($r/a \sim 0.8$). For 0.8 MA discharges, the line averaged density is around $0.6 \times 10^{20} \text{ m}^{-3}$. For 1.1 MA discharges, the line averaged density varies from 0.8 to $1.2 \times 10^{20} \text{ m}^{-3}$. From Fig. 15(b) the core ion temperature ($r/a \sim 0.4$) also responds linearly to the cooling. The change of core electron temperature is calculated as the temperature difference between before the cold pulse injection and around 5 ms after the cold pulse injection. The change of core ion temperature is calculated as the temperature difference between before and around 20 ms after the cold pulse injection.

The non-local effect is found to be correlated with the rotation reversal [20], shown in Fig. 16. For this 5.4 T, 0.8 MA discharge the line averaged density increased from $0.5 \times 10^{20} \text{ m}^{-3}$ to $1.0 \times 10^{20} \text{ m}^{-3}$. This density range covers both the LOC and SOC regimes, roughly indicated in colors of yellow and blue, respectively, based on previous C-Mod results. The rotation reversal from the co-current to the counter-current direction happens at a density around $0.8 \times 10^{20} \text{ m}^{-3}$. The interesting observation here is that the non-local effect disappears almost at the same density level. The core electron temperature increases as a result of the injection at 1.0 s, which is in the LOC regime and rotation is in the co-current direction. As the density rises, the core electron temperature decreases for the injection at 1.2 s. To illustrate the correlation, the energy confinement time, relative change of core electron temperature and absolute value of core plasma rotation are plotted as a function of line averaged density for 5.4 T, 0.8 MA discharges

in Fig. 17.

4. Transport Analysis

The electron heat diffusion coefficient χ_e has been calculated from power balance. Similar to the results in TEXT [1, 2, 3], RTP [6, 7, 8] etc, a rapid drop in the χ_e profile can explain the experimental results. Fig. 18(a) shows the LOC plasma diffusivity profiles averaged over three time intervals: before the injection, during the injection and after the injection. The CaF_2 was injected at 1.0 s for this discharge. The core diffusivity between $r/a = 0.3-0.8$ is reduced by $\sim 25\%$ during the injection, and it returns to the previous level around 40 ms after the injection. Fig. 18(b),(c) are time traces of the simulated core and edge electron temperatures based on this diffusive model. The red lines are measured electron temperatures. This drop of core transport looks like the formation of an internal transport barrier (ITB) during the cold pulse injection, and we do observe a reduction of density fluctuations as discussed in the previous section. For SOC plasmas where the non-local effect disappears, the reduction of core transport is not observed from this analysis.

An alternative model including a convection term in the heat flux ($q = -n_e\chi_e\nabla T_e + n_eVT_e$) can also match the observations and the result is shown in Fig. 19. The diffusivity is assumed to be constant during the cold pulse event, and the convection term is turned on right after the cold pulse injection. An inward pinch velocity profile (negative V) is obtained to match the experimental results. The simulated profiles agree with experiments as is shown in Fig. 19(b). Although one cannot distinguish between the two models, the Fourier analysis shown in Fig. 12 indicates that the pinch model is preferred.

The reduction of core transport during cold pulse injection in LOC plasmas is also observed in the saw-tooth induced heat pulse propagation, which is measured via soft X-ray brightness and time-to-peak as a function of radius. Time-to-peak is defined as the time delay from the sawtooth crash to the time with maximum brightness. Shown in Fig. 20(a) is soft X-ray brightness from a select number of channels for two sawtooth events of one LOC plasma shot: one is before the cold pulse injection (black, dashed line) and the other is right after the cold pulse injection (red, solid line). The time-to-peak is found to be larger after cold pulse injection, as shown in Fig. 20(b) where the time-to-peak radial profile is presented. The heat pulse diffusivity $\chi^{hp} \propto r^2/t_p$ [55] is found to be reduced by $\sim 30\%$ after the cold pulse injection, which is consistent with the transport calculation above.

5. Gyrokinetic simulation

Since the non-local effect is found to be correlated with the LOC/SOC transition, numerical studies of the turbulence characteristics for LOC and SOC plasmas were performed using the gyrokinetic code GYRO [56]. Shown in Fig. 21 are the smoothed

profiles of density (a), electron temperature (b) and ion temperature (c) in LOC (red solid lines) and SOC (blue dashed lines) plasmas. The gradients (d, e, f) are plotted as a/L , where L is the gradient length defined as $-X/\frac{\partial X}{\partial r}$, X could be n_e , T_e or T_i . The major difference in the gradients happens around $r/a = 0.8$, where a/L_{T_e} in LOC is slightly higher than in SOC; however a/L_{T_i} in LOC is significantly lower than in SOC. Linear gyrokinetic simulations are performed at two radii: $r/a = 0.5$ and $r/a = 0.75$. The input parameters of GYRO are listed in Table 1 and Table 2. Fig. 22 shows the results of real frequency (a) (c) and growth rate (b) (d) as a function of $k_\theta \rho_s$, for $r/a = 0.5$ (a) (b) and $r/a = 0.75$ (c) (d). k_θ is the poloidal wave number and $\rho_s = c_s/\Omega_i$ is the ion gyroradius with ion sound velocity $c_s = \sqrt{T_e/m_i}$. Red solid lines are for the LOC case and blue dashed lines are for the SOC case. Positive frequency indicates the modes propagate in the electron diamagnetic drift direction, and negative indicates the modes in the ion diamagnetic drift direction. At $r/a = 0.5$ both LOC and SOC plasmas are ITG dominant since the modes are in the ion diamagnetic direction for the range of $k_\theta \rho_s$ up to 1.0. At $r/a = 0.75$, for the SOC plasma, it is ITG dominant, but for the LOC plasma, the electron mode dominates. At this low wavenumber ($k_\theta \rho_s = 0 - 1.0$), it is TEM that will dominate for LOC plasmas. The difference of turbulence types for the outer part of LOC/SOC plasmas is consistent with previous simulation results [32] and recent experimental observations from CECE [36].

Table 1. The input values for linear GYRO simulation at $r/a = 0.50$

Parameters	LOC	SOC
$\langle n_e \rangle$ (10^{20} m^{-3})	0.58	1.05
Aspect ratio (R/a)	3.094857	3.094119
Elongation κ	1.212422	1.218704
$s_\kappa = (r/\kappa) \partial\kappa/\partial r$	0.055172	0.062530
Triangularity δ	0.059588	0.032149
$s_\delta = (r/\delta) \partial\delta/\partial r$	0.094592	0.101266
Safety factor q	1.229553	1.271063
$\hat{s} = (r/q) \partial q/\partial r$	0.943674	0.947398
$\nu_{e,i}/(c_s/a)$	0.035207	0.130783
Z_{eff}	3.6	1.75
T_i/T_e	0.615337	0.677205
n_i/n_e	0.687999	0.877835
a/L_{n_e}	0.485457	0.672722
a/L_{T_e}	2.619247	2.752895
a/L_{T_i}	1.674253	2.465612
$\eta_i = L_{n_i}/L_{T_i}$	3.448854	3.640865

To demonstrate the sensitivity of the turbulence to the driving terms a/L_{n_e} and a/L_{T_i} , linear simulations were performed over a range of this parameter space at $r/a = 0.75$, as shown in Fig. 23. For each point of $[a/L_{n_e}, a/L_{T_i}]$ the linear growth

Table 2. The input values for linear GYRO simulation at $r/a = 0.75$

Parameters	LOC	SOC
$\langle n_e \rangle (10^{20} \text{ m}^{-3})$	0.58	1.05
Aspect ratio (R/a)	3.081818	3.079783
Elongation κ	1.278817	1.289284
$s_\kappa = (r/\kappa) \partial\kappa/\partial r$	0.256387	0.262948
Triangularity δ	0.131257	0.137014
$s_\delta = (r/\delta) \partial\delta/\partial r$	0.324002	0.327953
Safety factor q	2.191458	2.252919
$\hat{s} = (r/q) \partial q/\partial r$	2.048509	1.992055
$\nu_{e,i}/(c_s/a)$	0.135773	0.475977
Z_{eff}	3.6	1.75
T_i/T_e	0.763729	0.675610
n_i/n_e	0.688001	0.877840
a/L_{n_e}	1.985225	1.937386
a/L_{T_e}	4.578889	3.864892
a/L_{T_i}	3.274659	3.899504
$\eta_i = L_{n_i}/L_{T_i}$	1.649495	2.01279

rate is calculated over $k_\theta \rho_s = 0 - 0.75$ and the maximum growth rate (most unstable mode) is chosen. The growth rate values normalized to c_s/a (a is the machine minor radius) are indicated by the contour lines. For the left-upper part of the contour plot, the linear growth rate is sensitive to the change of electron density gradients, which is a feature of TEMs. For the right-lower part of the contour plot, the linear growth rate is sensitive to the change of ion temperature gradients, which indicates the dominance of ITG modes. The plus signs are experimental values of the gradients. LOC plasmas (Fig. 23(a)) are in the TEM dominant regime, while SOC plasmas (23(b)) are in the ITG mode dominant regime.

6. Conclusions and discussions

Cold pulse injection experiments in Alcator C-Mod extend the understanding of the non-local phenomenon based on existing experiments from other machines. The measurement of ion temperature profiles could be used to verify various theoretical attempts to explain this non-local effect [57]. As seen with many other references, the transport analysis shows a reduction of core electron heat transport associated with the non-local effect, which is consistent with the fluctuation measurements. Fourier transformed profiles of the repetitive cold pulse injection experiments suggest the pure diffusive transport model is not valid for LOC discharges with the non-local effect, and an inward heat pinch should be responsible for this contradiction.

The non-local effect has a density/collisionality dependence. The results from

Alcator C-Mod experiments suggest that this dependence is correlated with the LOC/SOC transition density and rotation reversal critical density. One unified explanation for the existence of a transition density for apparently unrelated phenomena is the change of dominant turbulence types from TEMs in low collisional plasmas to ITG modes in high collisional plasmas [20]. This change requires that the electron collisional thermal coupling power is comparable to the power transport by TEMs. Experiments with direct electron heating (like ECRH on T-10 [58] and LH on Tore-Supra [59]) show that the confinement increases linearly with electron density when electron transport dominates. This dependence is weak with ion heating in ion transport loss dominant regimes [60]. This suggests the LOC regime is intrinsic to the electron mode dominated regimes, and the SOC regime is more likely to be ion mode dominant. The disappearance of electron channel non-local effect in SOC plasma can be the consequence that the coupling thermal power exceeds TEM transported power, which effectively eliminates the non-local effect in electron channel. The rotation reversal is suggested to be due to the change of sign in turbulent residual stress Π^{res} , whose gradient provides the torque. The sign of Π^{res} is predicted to change sign as the direction of turbulence propagation changes [61]. Linear gyrokinetic simulations show that at $r/a=0.75$ the LOC plasmas are TEM dominant, and the SOC plasmas are ITG mode dominant.

Acknowledgments

The authors thank J. Irby for electron density measurements, C. Fiore for neutron measurements, R. Parker, I. Hutchinson and J. Irby for physics operations and the Alcator C-Mod operations group for expert running of the tokamak. Work supported at MIT by US DoE Contract No DE-FC02-99ER54512 and in part by an appointment to the US DOE Fusion Energy Postdoctoral Research Program administered by ORISE. Computer simulations using GYRO were carried out on the MIT PSFC parallel AMD Opteron/Infiniband cluster Loki. Power balance and profile calculations were performed using TRANSP on the PPPL Unix cluster.

References

- [1] K. Gentle, W. Rowan, R. Bravenec, G. Cima, T. Crowley, H. Gasquet, G. Hallock, J. Heard, A. Ouroua, P. Phillips, *et al.*, “Strong nonlocal effects in a tokamak perturbative transport experiment,” *Physical review letters*, vol. 74, no. 18, pp. 3620–3623, 1995.
- [2] K. Gentle, R. Bravenec, G. Cima, H. Gasquet, G. Hallock, P. Phillips, D. Ross, W. Rowan, A. Wootton, T. Crowley, *et al.*, “An experimental counter-example to the local transport paradigm,” *Physics of Plasmas*, vol. 2, p. 2292, 1995.
- [3] K. Gentle, R. Bravenec, G. Cima, G. Hallock, P. Phillips, D. Ross, W. Rowan, A. Wootton, T. Crowley, A. Ouroua, *et al.*, “The evidence for nonlocal transport in the texas experimental tokamak,” *Physics of Plasmas*, vol. 4, p. 3599, 1997.
- [4] M. Kissick, J. Callen, E. Fredrickson, A. Janos, and G. Taylor, “Non-local component of electron heat transport in tfttr,” *Nuclear fusion*, vol. 36, no. 12, p. 1691, 1996.
- [5] M. Kissick, J. Callen, and E. Fredrickson, “Conditions and behaviour related to non-local electron heat transport on tfttr,” *Nuclear fusion*, vol. 38, no. 6, p. 821, 1998.

- [6] P. Mantica, P. Galli, G. Gorini, G. Hogeweij, J. De Kloe, N. Lopes Cardozo, and R. Team, “Nonlocal transient transport and thermal barriers in rijnhuizen tokamak project plasmas,” *Physical review letters*, vol. 82, no. 25, pp. 5048–5051, 1999.
- [7] P. Galli, G. Gorini, P. Mantica, G. Hogeweij, J. De Kloe, N. L. Cardozo, and R. Team, “non-local response of rtp ohmic plasmas to peripheral perturbations,” *Nuclear fusion*, vol. 39, no. 10, p. 1355, 1999.
- [8] G. Hogeweij, P. Mantica, G. Gorini, J. de Kloe, N. L. Cardozo, *et al.*, “Recording non-local temperature rise in the rtp tokamak,” *Plasma physics and controlled fusion*, vol. 42, no. 10, p. 1137, 2000.
- [9] F. Ryter, R. Neu, R. Dux, H.-U. Fahrback, F. Leuterer, G. Pereverzev, J. Schweinzer, J. Stober, W. Suttrop, A. U. Team, *et al.*, “Propagation of cold pulses and heat pulses in asdex upgrade,” *Nuclear fusion*, vol. 40, no. 11, p. 1917, 2000.
- [10] X. Zou, A. Geraud, P. Gomez, M. Mattioli, J. Ségui, F. Clairet, C. De Michelis, P. Devynck, T. D. de Wit, M. Erba, *et al.*, “Edge cooling experiments and non-local transport phenomena in tore supra,” *Plasma physics and controlled fusion*, vol. 42, no. 10, p. 1067, 2000.
- [11] P. Mantica, G. Gorini, F. Imbeaux, J. Kinsey, Y. Sarazin, R. Budny, I. Coffey, R. Dux, X. Garbet, L. Garzotti, *et al.*, “Perturbative transport experiments in jet low or reverse magnetic shear plasmas,” *Plasma physics and controlled fusion*, vol. 44, no. 10, p. 2185, 2002.
- [12] N. Tamura, S. Inagaki, K. Ida, T. Shimozuma, S. Kubo, T. Tokuzawa, K. Tanaka, S. Neudatchin, K. Itoh, D. Kalinina, *et al.*, “Observation of core electron temperature rise in response to an edge cooling in toroidal helical plasmas,” *Physics of plasmas*, vol. 12, p. 110705, 2005.
- [13] K. Ida, S. Inagaki, R. Sakamoto, K. Tanaka, H. Funaba, Y. Takeiri, K. Ikeda, C. Michael, T. Tokuzawa, H. Yamada, *et al.*, “Slow transition of energy transport in high-temperature plasmas,” *Physical review letters*, vol. 96, no. 12, p. 125006, 2006.
- [14] N. Tamura, S. Inagaki, K. Tanaka, C. Michael, T. Tokuzawa, T. Shimozuma, S. Kubo, R. Sakamoto, K. Ida, K. Itoh, *et al.*, “Impact of nonlocal electron heat transport on the high temperature plasmas of lhd,” *Nuclear fusion*, vol. 47, no. 5, p. 449, 2007.
- [15] K. Ida *et al.*, “Towards an emerging understanding of non-local transport,” *Nuclear Fusion*, in press.
- [16] K. Ida, Y. Sakamoto, H. Takenaga, N. Oyama, K. Itoh, M. Yoshinuma, S. Inagaki, T. Kobuchi, A. Isayama, T. Suzuki, *et al.*, “Transition between internal transport barriers with different temperature-profile curvatures in jt-60u tokamak plasmas,” *Physical review letters*, vol. 101, no. 5, p. 055003, 2008.
- [17] K. Ida, Y. Sakamoto, S. Inagaki, H. Takenaga, A. Isayama, G. Matsunaga, R. Sakamoto, K. Tanaka, S. Ide, T. Fujita, *et al.*, “Dynamic transport study of the plasmas with transport improvement in lhd and jt-60u,” *Nuclear Fusion*, vol. 49, no. 1, p. 015005, 2009.
- [18] H.-J. Sun, X.-T. Ding, L.-H. Yao, B.-B. Feng, Z.-T. Liu, X.-R. Duan, and Q.-W. Yang, “Experiment of non-local effect with smbi on hl-2a,” *Plasma Physics and Controlled Fusion*, vol. 52, no. 4, p. 045003, 2010.
- [19] H. Sun, P. Diamond, Z. Shi, C. Chen, L. Yao, X. Ding, B. Feng, X. Huang, Y. Zhou, J. Zhou, *et al.*, “Experimental evidence of the non-local response of transport to peripheral perturbations,” *Nuclear Fusion*, vol. 51, no. 11, p. 113010, 2011.
- [20] J. Rice, C. Gao, M. Reinke, P. Diamond, N. Howard, H. Sun, I. Cziegler, A. Hubbard, Y. Podpaly, W. Rowan, *et al.*, “Non-local heat transport, rotation reversals and up/down impurity density asymmetries in alcator c-mod ohmic l-mode plasmas,” *Nuclear Fusion*, vol. 53, no. 3, p. 033004, 2013.
- [21] R. R. Parker, M. Greenwald, S. Luckhardt, E. Marmor, M. Porkolab, and S. Wolfe, “Progress in tokamak research at mit,” *Nuclear fusion*, vol. 25, no. 9, p. 1127, 1985.
- [22] R. Bravenec, K. Gentle, P. Phillips, T. Price, W. Rowan, K. Empson, W. Hodge, C. Klepper, T. Kochanski, D. Patterson, *et al.*, “Confinement time scaling in text,” *Plasma physics and controlled fusion*, vol. 27, no. 11, p. 1335, 1985.

- [23] Y. Shimomura, N. Suzuki, and M. Sugihara, “Empirical scaling of energy confinement time of l-mode and optimized mode and some consideration of reactor core plasma in tokamak,” *Rep./Japan atomic energy inst.*, vol. 1000, pp. 87–080, 1987.
- [24] F. Söldner, E. Müller, F. Wagner, H. Bosch, A. Eberhagen, H. Fahrbach, G. Fussmann, O. Gehre, K. Gentle, J. Gernhardt, *et al.*, “Improved confinement in high-density ohmic discharges in asdex,” *Physical review letters*, vol. 61, no. 9, pp. 1105–1108, 1988.
- [25] X. Garbet, J. Payan, C. Laviron, P. Devynck, S. Saha, H. Capes, X. Chen, J. Coulon, C. Gil, G. Harris, *et al.*, “Turbulence and energy confinement in tore supra ohmic discharges,” *Nuclear fusion*, vol. 32, no. 12, p. 2147, 1992.
- [26] F. Ryter, K. Buchl, C. Fuchs, O. Gehre, O. Gruber, A. Herrmann, A. Kallenbach, M. Kaufmann, W. Koppendorfer, F. Mast, *et al.*, “H-mode results in asdex upgrade,” *Plasma physics and controlled fusion*, vol. 36, no. 7A, p. A99, 1994.
- [27] G. Bracco and K. Thomsen, “Analysis of a global energy confinement database for jet ohmic plasmas,” *Nuclear fusion*, vol. 37, no. 6, p. 759, 1997.
- [28] C. Rettig, T. Rhodes, J. Leboeuf, W. Peebles, E. Doyle, G. Staebler, K. Burrell, and R. Moyer, “Search for the ion temperature gradient mode in a tokamak plasma and comparison with theoretical predictions,” *Physics of Plasmas*, vol. 8, p. 2232, 2001.
- [29] M. Greenwald, N. Basse, P. Bonoli, R. Bravenec, E. Edlund, D. Ernst, C. Fiore, R. Granetz, A. Hubbard, J. Hughes, *et al.*, “Confinement and transport research in alcator c-mod,” *Fusion science and technology*, vol. 51, no. 3, pp. 266–287, 2007.
- [30] L. Lin, M. Porkolab, E. Edlund, J. Rost, M. Greenwald, N. Tsujii, J. Candy, R. Waltz, and D. Mikkelsen, “Studies of turbulence and transport in alcator c-mod ohmic plasmas with phase contrast imaging and comparisons with gyrokinetic simulations,” *Plasma Physics and Controlled Fusion*, vol. 51, no. 6, p. 065006, 2009.
- [31] J. Rice, I. Cziegler, P. Diamond, B. Duval, Y. Podpaly, M. Reinke, P. Ennever, M. Greenwald, J. Hughes, Y. Ma, *et al.*, “Rotation reversal bifurcation and energy confinement saturation in tokamak ohmic l-mode plasmas,” *Physical Review Letters*, vol. 107, no. 26, p. 265001, 2011.
- [32] J. Rice, M. Greenwald, Y. Podpaly, M. Reinke, P. Diamond, J. Hughes, N. Howard, Y. Ma, I. Cziegler, B. Duval, *et al.*, “Ohmic energy confinement saturation and core toroidal rotation reversal in alcator c-mod plasmas,” *Physics of Plasmas*, vol. 19, p. 056106, 2012.
- [33] B. Duval, A. Bortolon, A. Karpushov, R. Pitts, A. Pochelon, A. Scarabosio, *et al.*, “Bulk plasma rotation in the tcv tokamak in the absence of external momentum input,” *Plasma Physics and Controlled Fusion*, vol. 49, no. 12B, p. B195, 2007.
- [34] J. Rice, A. Ince-Cushman, M. Reinke, Y. Podpaly, M. Greenwald, B. LaBombard, and E. Marmor, “Spontaneous core toroidal rotation in alcator c-mod l-mode, h-mode and itb plasmas,” *Plasma Physics and Controlled Fusion*, vol. 50, no. 12, p. 124042, 2008.
- [35] N. Uckan, *ITER physics design guidelines: 1989*. International Atomic Energy Agency, 1990.
- [36] C. Sung, A. White, N. Howard, C. Oi, J. Rice, C. Gao, P. Ennever, M. Porkolab, F. Parra, *et al.*, “Changes in core electron temperature fluctuations across the ohmic energy confinement transition in alcator c-mod plasmas,” *Nuclear fusion*, vol. 53, p. 083010, 2013.
- [37] E. S. Marmor, “The alcator c-mod program,” *Fusion science and technology*, vol. 51, no. 3, pp. 261–265, 2007.
- [38] N. Howard, M. Greenwald, and J. Rice, “Characterization of impurity confinement on alcator c-mod using a multi-pulse laser blow-off system,” *Review of Scientific Instruments*, vol. 82, no. 3, pp. 033512–033512, 2011.
- [39] N. Basse, A. Dominguez, E. Edlund, C. Fiore, R. Granetz, A. Hubbard, J. Hughes, I. Hutchinson, J. Irby, B. LaBombard, *et al.*, “Diagnostic systems on alcator c-mod,” *Fusion science and technology*, vol. 51, no. 3, pp. 476–507, 2007.
- [40] R. Watterson and K.-i. Chen, “Status of the alcator c-mod scanning two-dimensional thomson scattering diagnostic,” *Review of Scientific Instruments*, vol. 61, no. 10, pp. 2867–2869, 1990.
- [41] D. A. Mossessian, A. Hubbard, and J. Irby, “Performance of alcator c-mod core thomson scattering

- system,” *Review of scientific instruments*, vol. 70, no. 1, pp. 759–762, 1999.
- [42] J. W. Hughes, D. Mossessian, A. Hubbard, E. Marmor, D. Johnson, and D. Simon, “High-resolution edge thomson scattering measurements on the alcator c-mod tokamak,” *Review of Scientific Instruments*, vol. 72, no. 1, pp. 1107–1110, 2001.
- [43] J. W. Hughes, D. Mossessian, K. Zhurovich, M. DeMaria, K. Jensen, and A. Hubbard, “Thomson scattering upgrades on alcator c-mod,” *Review of scientific instruments*, vol. 74, no. 3, pp. 1667–1670, 2003.
- [44] J. Irby, E. Marmor, E. Sevillano, and S. Wolfe, “Two-color interferometer system for alcator c-mod,” *Review of Scientific Instruments*, vol. 59, no. 8, pp. 1568–1570, 1988.
- [45] A. Ince-Cushman, J. Rice, M. Bitter, M. Reinke, K. Hill, M. Gu, E. Eikenberry, C. Broennimann, S. Scott, Y. Podpaly, *et al.*, “Spatially resolved high resolution x-ray spectroscopy for magnetically confined fusion plasmas,” *Review of Scientific Instruments*, vol. 79, no. 10, pp. 10E302–10E302, 2008.
- [46] M. Reinke, Y. Podpaly, M. Bitter, I. Hutchinson, J. Rice, L. Delgado-Aparicio, C. Gao, M. Greenwald, K. Hill, N. Howard, *et al.*, “X-ray imaging crystal spectroscopy for use in plasma transport research,” *Review of Scientific Instruments*, vol. 83, no. 11, pp. 113504–113504, 2012.
- [47] M. Porkolab, J. C. Rost, N. Basse, J. Dorris, E. Edlund, L. Lin, Y. Lin, and S. Wukitch, “Phase contrast imaging of waves and instabilities in high temperature magnetized fusion plasmas,” *Plasma Science, IEEE Transactions on*, vol. 34, no. 2, pp. 229–234, 2006.
- [48] L. Lin, E. Edlund, M. Porkolab, Y. Lin, and S. Wukitch, “Vertical localization of phase contrast imaging diagnostic in alcator c-mod,” *Review of scientific instruments*, vol. 77, no. 10, pp. 10E918–10E918, 2006.
- [49] Y. Lin, *Experimental application and numerical study of reflectometry in the Alcator C-Mod tokamak*. Plasma Science and Fusion Center, Massachusetts Institute of Technology, 2001.
- [50] N. Lopes Cardozo, “Perturbative transport studies in fusion plasmas,” *Plasma physics and controlled fusion*, vol. 37, no. 8, pp. 799–852, 1995.
- [51] A. Jacchia, P. Mantica, F. De Luca, and G. Gorini, “Determination of diffusive and nondiffusive transport in modulation experiments in plasmas,” *Physics of Fluids B: Plasma Physics*, vol. 3, no. 11, pp. 3033–3040, 1991.
- [52] T. D. de Wit, M. Erba, M. Mattioli, and J.-L. Ségui, “Self-consistent removal of sawtooth oscillations from transient plasma data by generalized singular value decomposition,” *Physics of Plasmas*, vol. 5, p. 1360, 1998.
- [53] S. Inagaki, N. Tamura, T. Tokuzawa, K. Ida, T. Kobayashi, T. Shimozuma, S. Kubo, H. Tsuchiya, Y. Nagayama, K. Kawahata, *et al.*, “Fluctuations with long-distance correlation in quasi-stationary and transient plasmas of lhd,” *Nuclear Fusion*, vol. 52, no. 2, p. 023022, 2012.
- [54] C. Sung, A. White, J. Irby, R. Leccacorvi, R. Vieira, C. Oi, W. Peebles, and X. Nguyen, “Design of a correlation electron cyclotron emission diagnostic for alcator c-mod,” *Review of Scientific Instruments*, vol. 83, no. 10, pp. 10E311–10E311, 2012.
- [55] J. Callen and G. Jahns, “Experimental measurement of electron heat diffusivity in a tokamak,” *Physical Review Letters*, vol. 38, pp. 491–494, 1977.
- [56] J. Candy and R. Waltz, “An eulerian gyrokinetic-maxwell solver,” *Journal of Computational Physics*, vol. 186, no. 2, pp. 545–581, 2003.
- [57] J. Kinsey, R. Waltz, and H. S. John, “Theoretical transport modeling of ohmic cold pulse experiments,” *Physics of Plasmas*, vol. 5, p. 3974, 1998.
- [58] V. B. Alikhaev, N. Vasin, Y. Esipchuk, A. Kislov, G. Noikin, and K. Razamova, “Energy confinement in the plasma of the t-10 tokamak,” *Sov. J. Plasma Phys*, vol. 13, pp. 1–10, 1987.
- [59] G. T. Hoang, C. Gil, E. Joffrin, D. Moreau, A. Becoulet, P. Bibet, J. Bizarro, R. Budny, J. Carrasco, J. Coulon, *et al.*, “Improved confinement in high li lower hybrid driven steady state plasmas in tore supra,” *Nuclear fusion*, vol. 34, no. 1, p. 75, 1994.
- [60] M. Wakatani, V. Mukhovatov, K. Burrell, J. Connor, J. Cordey, Y. V. Esipchuk, X. Garbet, S. Lebedev, M. Mori, K. Toi, *et al.*, “Chapter 2: Plasma confinement and transport,” *Nuclear*

Fusion, vol. 39, no. 12, pp. 2175–2249, 1999.

- [61] P. Diamond, C. McDevitt, Ö. Gürçan, T. Hahm, W. Wang, E. Yoon, I. Holod, Z. Lin, V. Naulin, and R. Singh, “Physics of non-diffusive turbulent transport of momentum and the origins of spontaneous rotation in tokamaks,” *Nuclear Fusion*, vol. 49, no. 4, p. 045002, 2009.

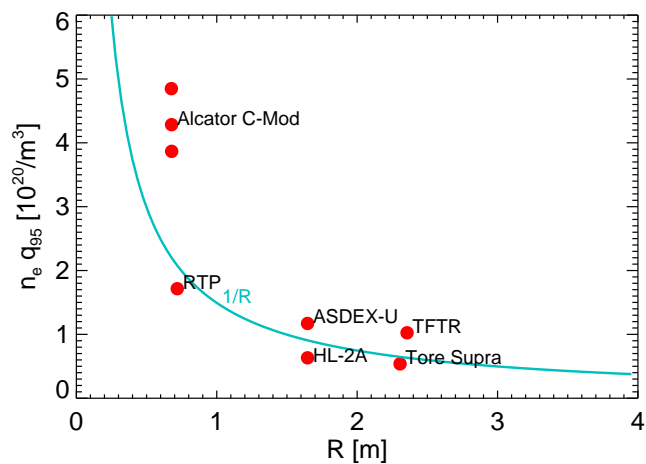


Figure 1. The product of cutoff density for non-local effect and q_{95} as a function of major radius for different devices [5, 7, 9, 10, 19, 20]. The solid line represents $1/R$.

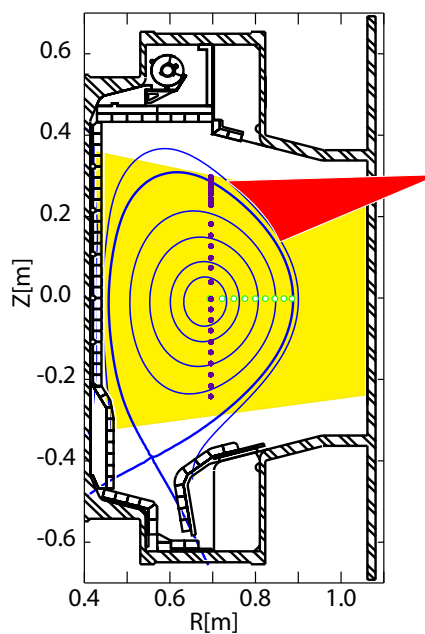


Figure 2. The cross section of Alcator C-Mod with lower single null equilibrium. Blue lines are poloidal magnetic flux contours; the red area indicates the approximate location of LBO injected impurities; the yellow area indicates the viewing range of a high resolution imaging x-ray spectrometer; horizontal green open circles represent the ECE measurement positions; vertical purple filled circles are Thomson scattering measurement positions.

Figure

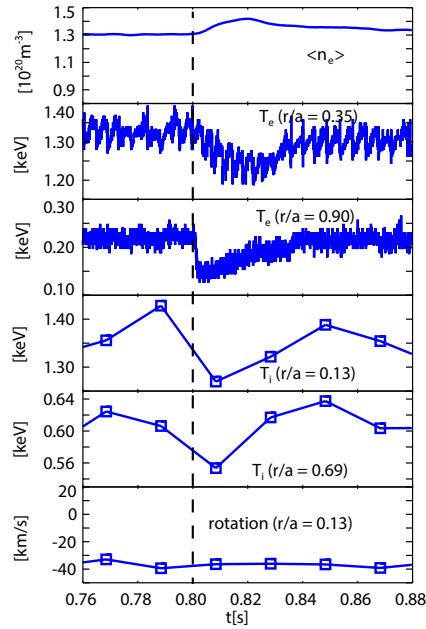


Figure 3. Time traces of line averaged electron density, electron temperatures at $r/a = 0.35$ and $r/a = 0.90$, ion temperatures at $r/a = 0.13$ and $r/a = 0.69$, core plasma rotation for an SOC discharge. The CaF_2 is injected at 0.8 s.

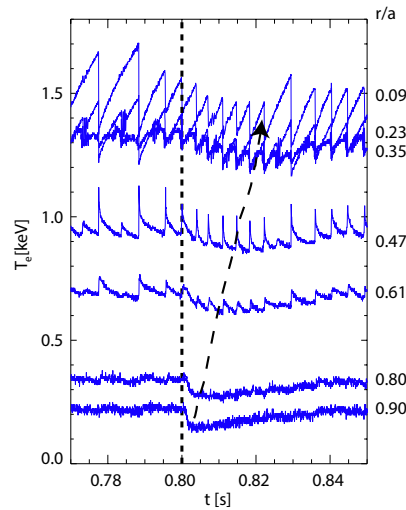


Figure 4. Same discharge as in Fig. 3. Time trace of electron temperatures at different radii measured by GPC1. The arrow shows the trajectory of minima in the electron temperature from each channel. The evolution of peaks at different radii clearly shows the diffusive behavior of the cold front propagation.

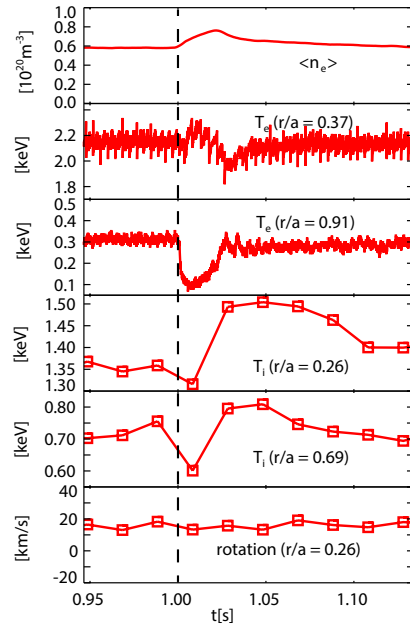


Figure 5. Time traces of line averaged electron density, electron temperatures at $r/a = 0.37$ and $r/a = 0.91$, ion temperatures at $r/a = 0.26$ and $r/a = 0.69$, core plasma rotation for an LOC discharge. The CaF_2 is injected at 1.0 s.

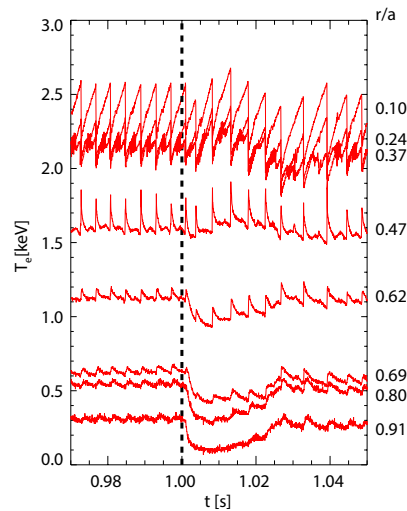


Figure 6. Same discharge as in Fig. 5. The evolution of peaks in core channels indicates the non-diffusive heat transport.

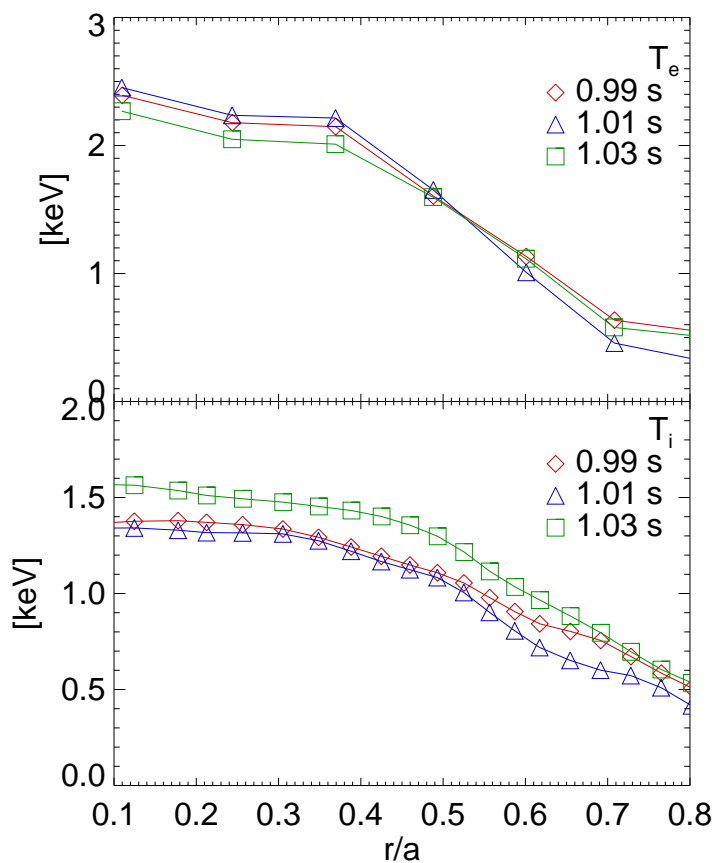


Figure 7. Same discharge as in Fig. 5. The profile evolution of the electron (top) and ion (bottom) temperatures for an LOC discharge. The injection time is 1.0 s.

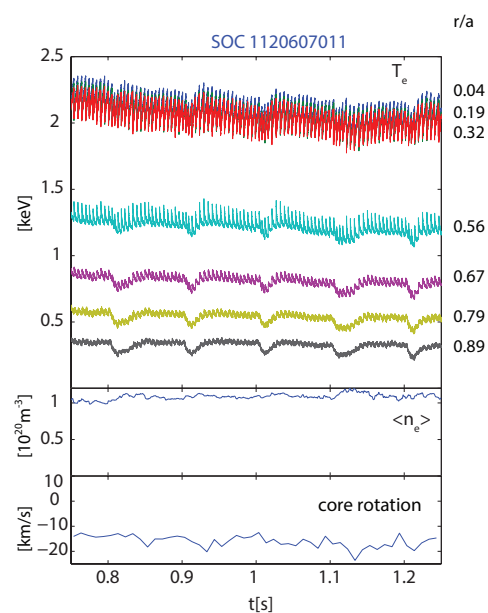


Figure 8. Time traces of electron temperatures, line averaged electron density and core plasma rotation for an SOC discharge with repetitive LBO injections at 0.8 s, 0.9 s, 1.0 s, 1.1 s and 1.2 s.

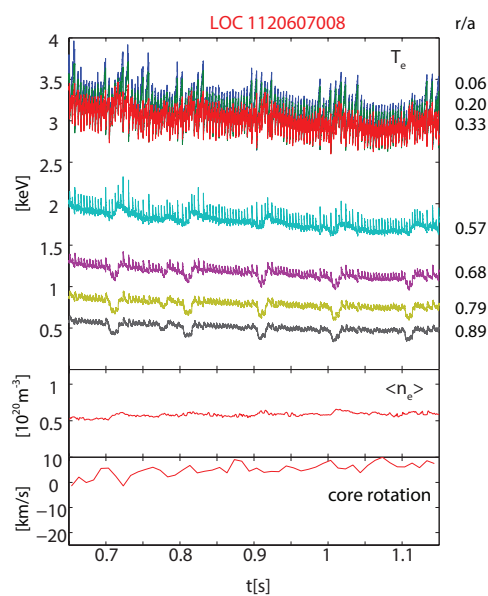


Figure 9. Time traces of electron temperatures, line averaged electron density and core plasma rotation for an LOC discharge with repetitive LBO injections at 0.7 s, 0.8 s, 0.9 s, 1.0 s and 1.1 s.

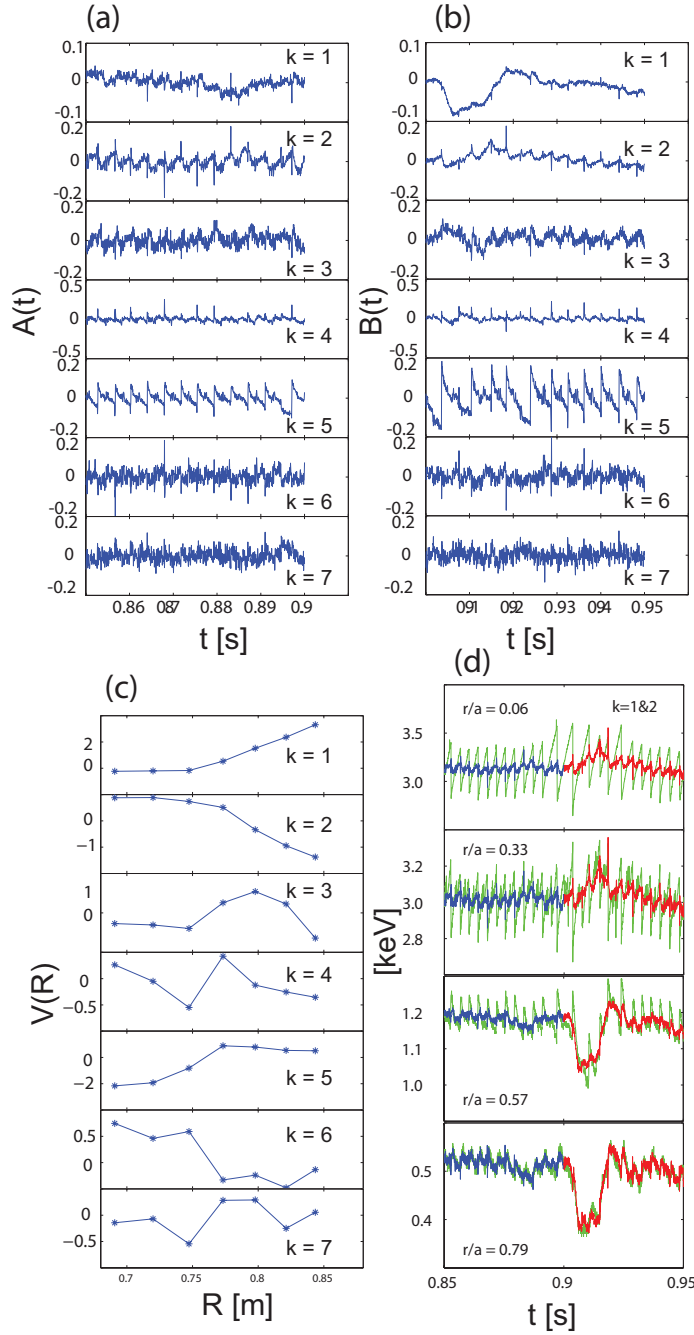


Figure 10. The seven modes associated with the GSVD for the LOC discharge of Fig. 9. (a): the temporal modes $A_k(t)$ of sawtooth subset; (b): the temporal modes $B_k(t)$ of perturbation subset; (c) the common spatial modes $V_k(R)$; (d) the evolution of reconstructed electron temperatures by choosing the first two dominant modes ($k=1,2$) at different radii. Green lines are original signals, blue and red lines are reconstructed signals before and after the cold pulse injection, respectively.

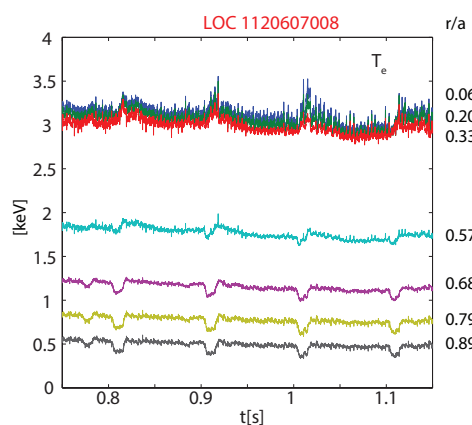


Figure 11. Time traces of electron temperatures in Fig. 9 with GSVD applied for LOC discharge.

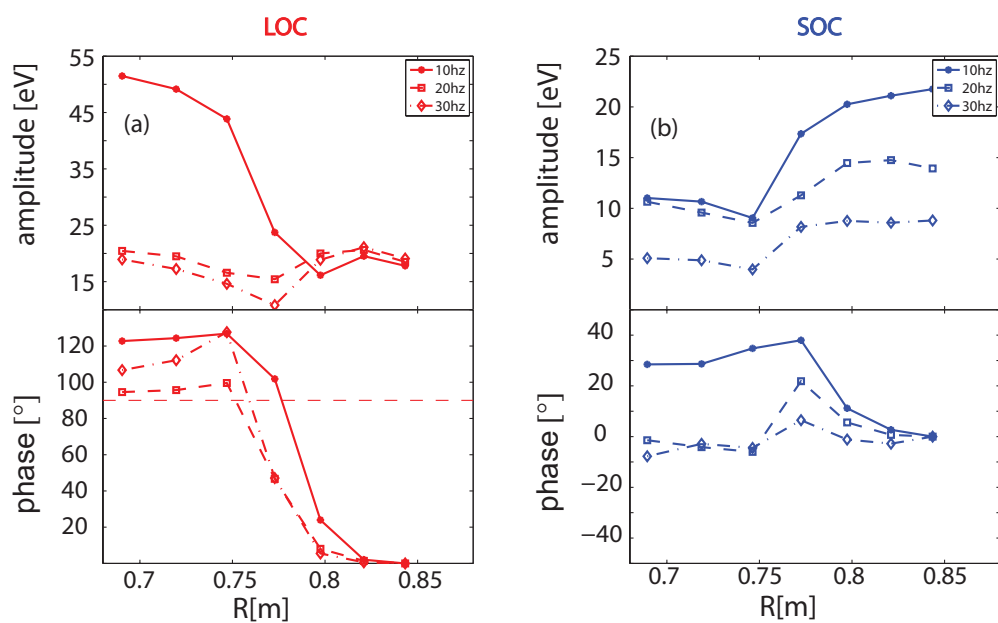


Figure 12. The FFT amplitude and phase profiles for (a) LOC discharge in Fig. 9 with GSVD applied, and (b) SOC discharge in Fig. 8 with GSVD applied.

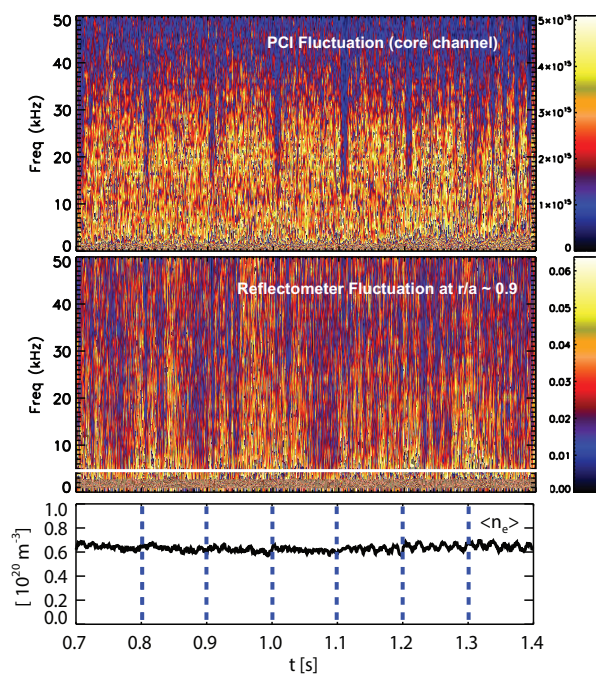


Figure 13. The LOC discharge in Fig. 9. Top frame: density fluctuation measurement from PCI; middle frame: edge density fluctuation measurement from reflectometer; bottom frame: line integrated electron density with dashed lines indicating the LBO injection times.

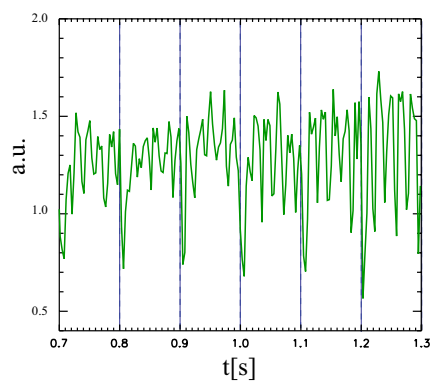


Figure 14. Time trace of the spectral power integrated over 10 - 40 kHz from PCI in Fig. 13. The spectral power trace is averaged over 1.6 ms.

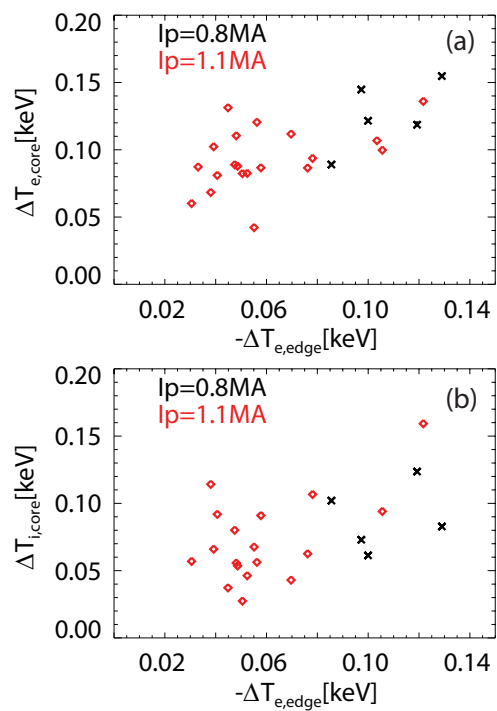


Figure 15. The changes of the core electron temperature (a) and core ion temperature (b) vs. the changes of edge electron temperature for 0.8 MA (black crosses) and 1.1 MA (red diamonds).

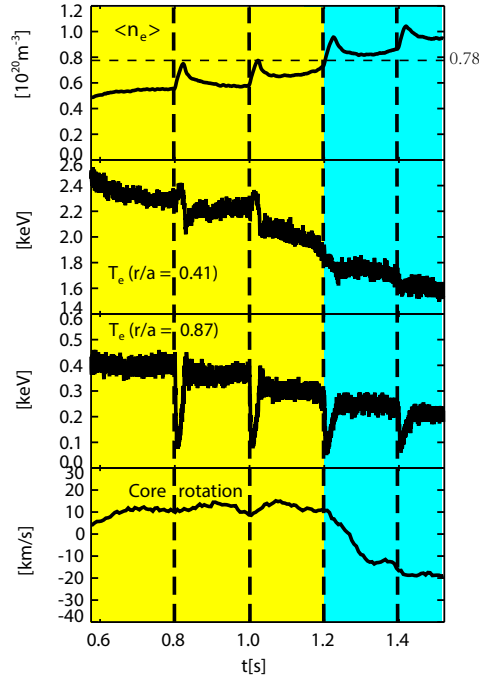


Figure 16. From top to bottom: time traces of line averaged electron density, core electron temperature, edge electron temperature and core rotation for a density ramp-up discharge. The yellow color indicates the LOC regime, and blue color indicates the SOC regime.

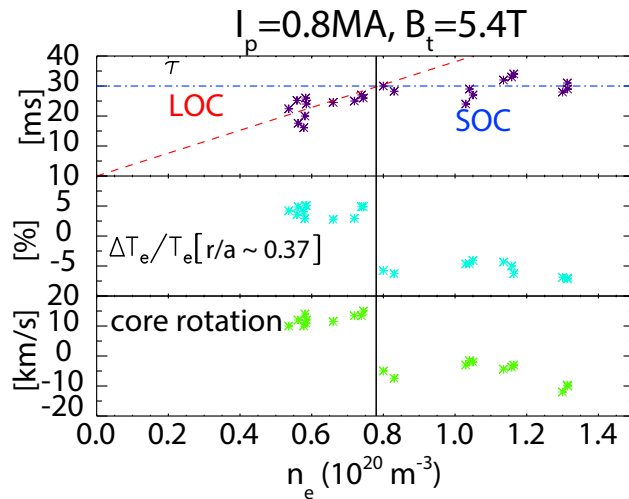


Figure 17. From top to bottom: energy confinement time, relative change of core electron temperature, absolute value of core rotation vs. line averaged electron density. The vertical line indicates the LOC-SOC transition density $n_{e,20} \sim 0.78$.

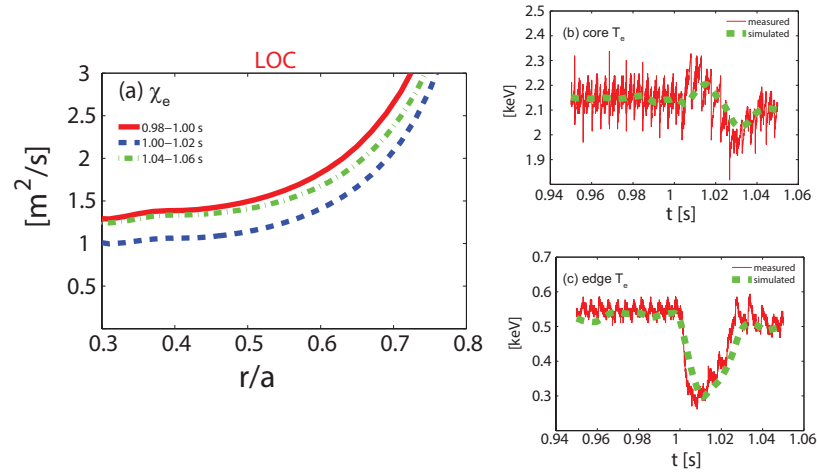


Figure 18. Left: The electron heat diffusivity profiles before (red solid line), during (blue dashed line) and 40 ms after (green dash-dot line) the LBO injection for a LOC plasma. Right: The time traces of measured (red solid lines) and simulated (green dashed lines) for core (b) and edge (c) electron temperatures.

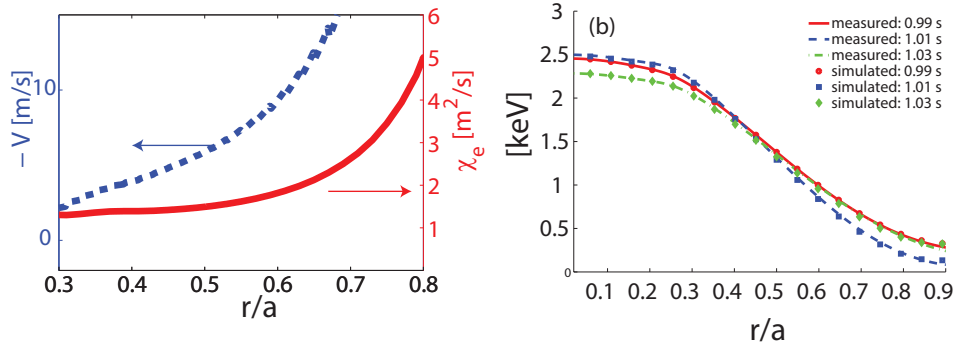


Figure 19. Left: The χ_e (red, solid line) and $-V$ (blue, dashed line) profiles. Right: The measured T_e profiles at 0.99 s (red, solid line), 1.013 s (blue dashed line) 1.03 s (green, dash-dot line); and the simulated T_e profiles at 0.99 s (red, circles), 1.013 s (blue squares) 1.03 s (green, diamonds). The LBO injection time is 1.0 s.

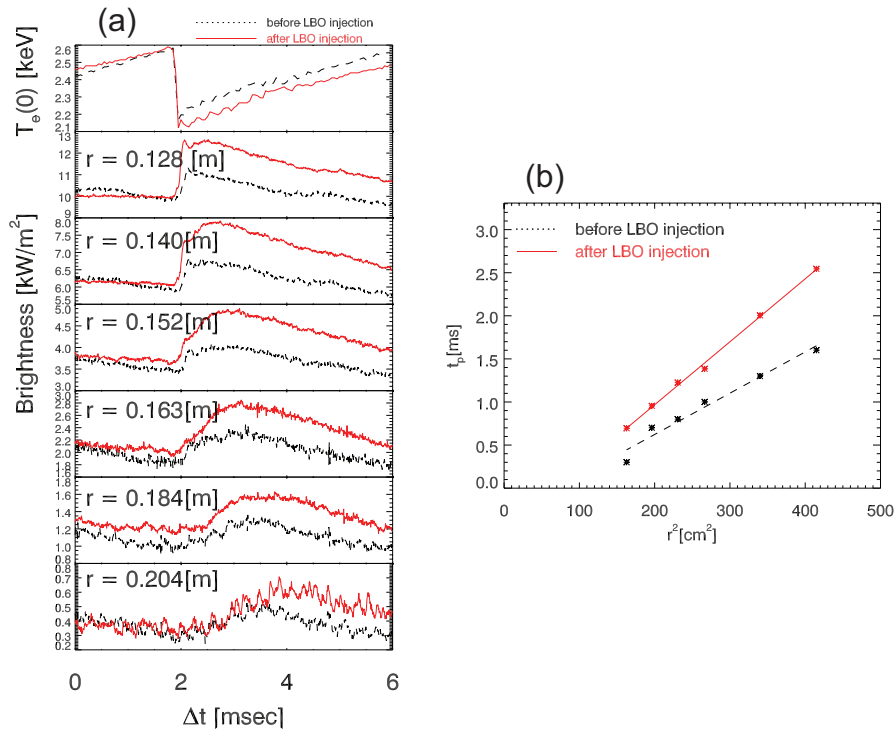


Figure 20. Comparison of (a) soft X-ray brightness chords and (b) time-to-peak during two sawtooth-induced heat pulses before (black, dashed lines) and after (red, solid lines) the LBO injection for a LOC plasma.

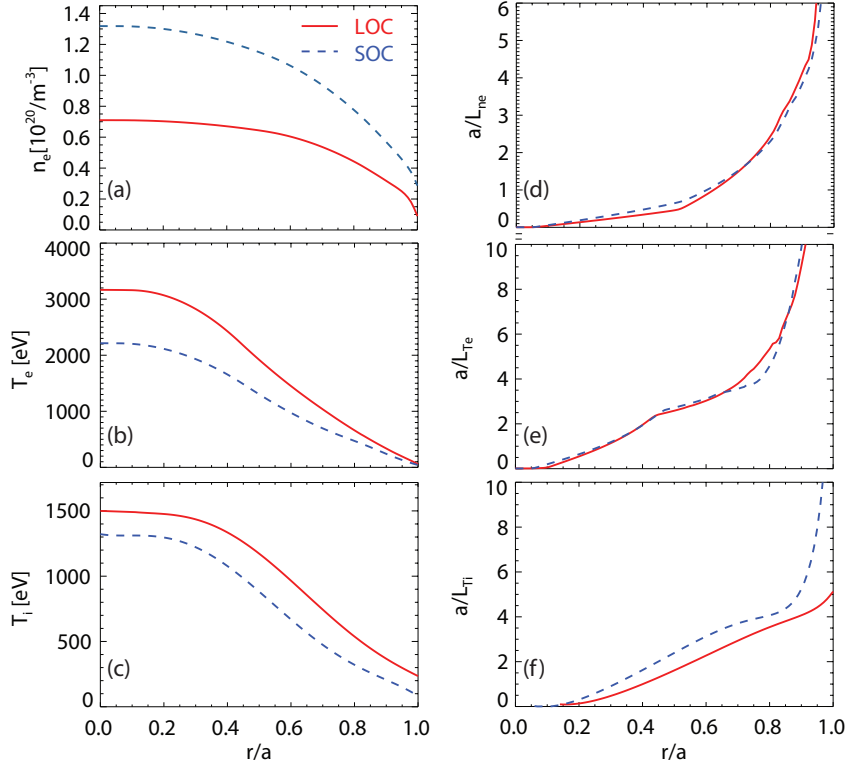


Figure 21. Profiles of electron density (a), electron temperature (b), ion temperature (c) and their gradients (d)(e)(f) for LOC (red solid lines) and SOC (blue dashed lines) discharges.

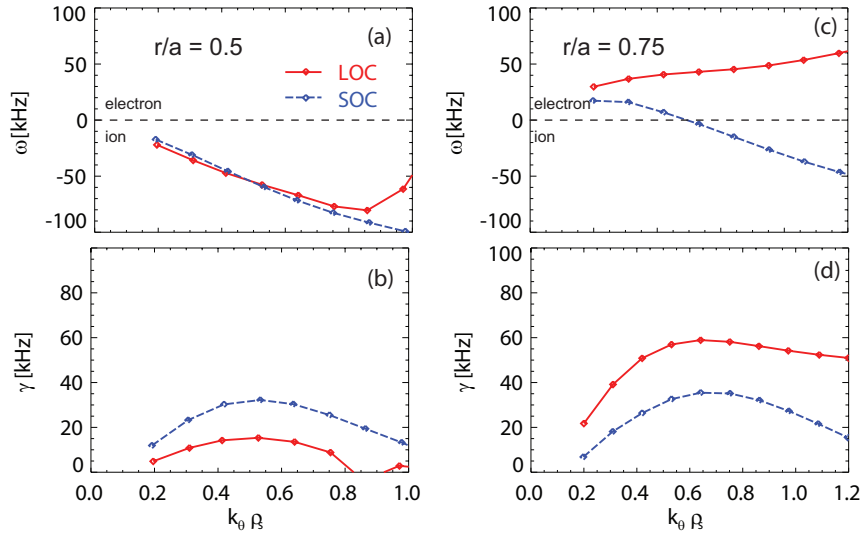


Figure 22. The real frequency (a)(c) and growth rate (b)(d) at $r/a = 0.5$ (a)(b) and $r/a = 0.75$ (c)(d) for LOC (red solid lines) and SOC (blue dashed lines) discharges. Positive real frequency indicates the modes in the electron diamagnetic direction, negative real frequency indicates the modes in the ion diamagnetic direction.

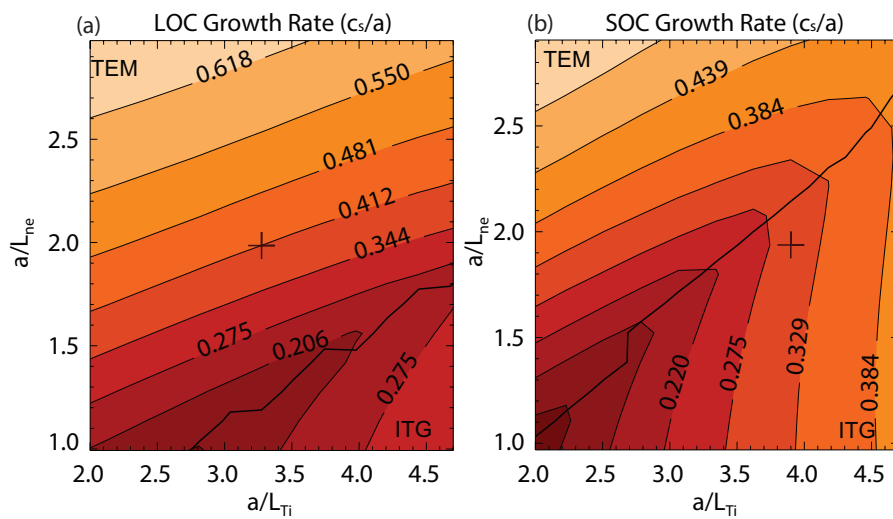


Figure 23. Contour plot of linear growth rate as a function of a/L_{Ti} and a/L_{ne} for an LOC plasma (a) and an SOC plasma (b) at $r/a = 0.75$. The cross signs indicate the experimental values.